Magnetic moments of the first excited 2^+ states in the semi-magic ^{112,114,116,122,124}Sn isotopes

J. Walker,[1,2] A. Jungclaus,[1] J. Leske,[3] K.-H. Speidel,[4] A. Ekström,[5,*] P. Boutachkov,[6] J. Cederkäll,[5] P. Doornenbal,[7,†] J. Gerl,[6] R. Gernhäuser,[8] N. Goel,[6] M. Górska,[6] I. Kojouharov,[6] P. Maier-Komor,[8] V. Modamio,[1] F. Naqvi,[6,9] N. Pietralla,[3] S. Pietri,[6] W. Prokopowicz,[6] H. Schaffner,[6] R. Schwengner,[10] and H.-J. Wollersheim[6]

[1]*Instituto de Estructura de la Materia, CSIC, E-28006 Madrid, Spain*
[2]*Departamento de Física Teórica, Universidad Autónoma de Madrid, E-28049 Madrid, Spain*
[3]*Institut für Kernphysik, Technische Universität Darmstadt, D-64289 Darmstadt, Germany*
[4]*Helmholtz-Institut für Strahlen- und Kernphysik, Universität Bonn, D-53115 Bonn, Germany*
[5]*Department of Physics, Lund University, S-22100 Lund, Sweden*
[6]*Gesellschaft für Schwerionenforschung, D-64291 Darmstadt, Germany*
[7]*RIKEN Nishina Center, Wako, Saitama 351-0198, Japan*
[8]*Physik Department E12, Technische Universität München, D-85748 Garching, Germany*
[9]*Institut für Kernphysik, Universität zu Köln, D-50937 Köln, Germany*
[10]*Institut für Strahlenphysik, Helmholtz-Zentrum Dresden Rossendorf, D-01314 Dresden, Germany*

(Received 5 April 2011; published 19 July 2011)

The g factors of the first excited 2^+ states in the ^{112,114,116,122,124}Sn isotopes have been measured with high accuracy using the transient field technique in combination with Coulomb excitation in inverse kinematics. The experimental results are discussed in a qualitative way on the basis of empirical single-particle g factors of the relevant proton and neutron orbitals and are compared to a number of different theoretical calculations. The results are found to be best described by shell-model calculations in an extended configuration space. Clear evidence for the contribution of neutron pair excitations from the $1d_{3/2}$ to the $0h_{11/2}$ orbital to the wave function of the 2_1^+ state in ^{122,124}Sn has been obtained.

DOI: 10.1103/PhysRevC.84.014319 PACS number(s): 21.10.Ky, 21.60.Cs, 27.60.+j

I. INTRODUCTION

The chain of semi-magic Sn isotopes plays a special role in low-energy nuclear structure research because it provides experimental information on all 33 isotopes over a full major neutron shell, from the $N = Z$ nucleus ^{100}Sn up to ^{132}Sn and even beyond. From the theoretical point of view, it allows us to study the evolution of the nuclear structure from the neutron-deficient regime close to the proton drip line via the valley of stability up to neutron-rich regions ten neutrons above the heaviest stable isotope. The Sn isotopes are an ideal test ground for the study of pairing correlations in mean-field approaches as well as the evolution of empirical single-particle energies from the closed-shell nucleus ^{100}Sn to single-hole energies in ^{132}Sn in the framework of the nuclear shell model.

Since the early work of Talmi [1,2], the Sn isotopes have been considered to be a good example for the approximate validity of the generalized seniority scheme, mainly based on the observation of nearly constant excitation energies of the first excited 2^+ states across the entire major $N = 50$–82 neutron shell and the strong pairing correlations in these semi-magic nuclei. However, in a series of recent measurements of $E2$ strength in the Sn isotopes in the lower half of the major shell, namely, in neutron-deficient and stable $^{106-114}$Sn, a deviation from the behavior suggested by the simple seniority scheme has been observed [3–9]. The latter and the modern large-scale shell-model calculations predict a maximum in $E2$ strength around midshell and a symmetric parabolic decrease toward both the $N = 50$ and $N = 82$ shell closures [3,8]. While such a behavior has indeed been observed in the upper half of the shell, from ^{116}Sn up to ^{132}Sn, an unexpected increase in $E2$ strengths has been reported between the midshell isotope ^{116}Sn and its lighter neighbor, ^{114}Sn [7], with the values then staying nearly constant within the experimental uncertainties down to ^{106}Sn [3–6,8,9].

One of the arguments put forward as a possible explanation for the observed excess of $E2$ strength in the neutron-deficient Sn isotopes is the increasing importance of proton-core excitations with decreasing neutron number [3,8]. The magnetic moment of the 2_1^+ state is probably one of the most sensitive probes to measure the contribution of proton-core-excited configurations, such as $0g_{9/2}^{-1}1d_{5/2}$, to the wave function of this state. The empirical single-particle g factors of the neutron orbitals $d_{5/2}$ and $g_{7/2}$, predominantly filled in the neutron-deficient Sn isotopes, are either negative or small ($g = -0.43$ for $d_{5/2}$ and $g = +0.18$ for $g_{7/2}$), whereas the proton orbitals most relevant for the proton core excitations, namely, $g_{9/2}$ below and $d_{5/2}$ above $Z = 50$, have large positive g factors ($+$ 1.22 and $+$ 1.38, respectively). Unfortunately, magnetic moment measurements for short-lived excited states using radioactive beams are still challenging. However, as in the Sn isotopic chain the increase in $E2$ strengths has been observed in the region of stable isotopes, namely, between midshell isotope ^{116}Sn and its lighter neighbor, ^{114}Sn, stable beam magnetic moment measurements can possibly contribute to a better understanding of the observed behavior. Two such experiments have been performed for all stable Sn isotopes in the past,

*Present address: Department of Physics, University of Oslo, Oslo, Norway.
†Present address: RIKEN, Nishina Center, Wako, Saitama, Japan.

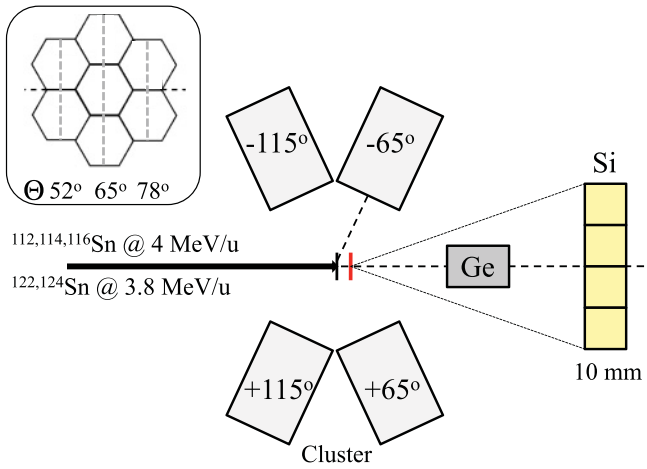

FIG. 1. (Color online) Sketch of the experimental setup used in the experiments. The γ radiation is detected in four EUROBALL cluster detectors positioned at $\pm 65^\circ$ and $\pm 115^\circ$ with respect to the beam axis in coincidence with charged particles detected in an array of four Si diodes.

using in both cases the transient field technique after Coulomb excitation in normal kinematics [10,11]. However, due to the limited accuracy achieved in these experiments, we decided to remeasure the 2_1^+ g factors in some stable Sn isotopes, namely, ^{112,114,116,122,124}Sn, under improved experimental conditions, aiming for a significantly higher precision of the final results. To achieve this goal we used the transient field technique in combination with Coulomb excitation in inverse kinematics and a very powerful γ-ray detection setup consisting of four EUROBALL cluster detectors (in total, 28 Ge crystals) positioned in a horizontal plane.

II. THE EXPERIMENTAL SETUP

Two experiments have been performed at the UNILAC accelerator of the Gesellschaft für Schwerionenforschung (GSI). In the first, beams of ^{112,114,116}Sn at energies of 4.0 MeV/u and, in the second, beams of ^{122}Sn and ^{124}Sn at 3.8 MeV/u were used with nearly identical experimental setups, as sketched in Fig. 1. The beam particles were Coulomb excited on the first layer of a multilayer target consisting of 0.67 mg/cm^2 (0.66 mg/cm^2 in the ^{122,124}Sn runs) natural carbon. The excited ions then experienced a transient magnetic field during their passage through a 10.8 (10.9) mg/cm^2 ferromagnetic natural Gd layer before traversing 1.0 (1.0) mg/cm^2 Ta and finally stopping in a 4.86 (5.23) mg/cm^2 Cu layer. This multilayer target was cooled by liquid nitrogen to well below the Curie temperature of Gd ($T_C = 290$ K) and polarized by a vertical magnetic field of 80 mT, the direction of which was reversed every 3 min. A thick Ta foil was mounted behind the target to stop the beam particles. Four Si diodes (1 cm $\times$ 1 cm each) were placed 30 mm (27 mm) downstream above and below the beam axis to detect the forward-scattered C target ions in the angular ranges of 2°–20° and 23°–38°, respectively (2°–22° and 26°–40°, respectively). The γ rays emitted from the excited states populated in the Coulomb excitation of the Sn projectiles on the C target layer were detected in coincidence with the C ions in four EUROBALL cluster detectors, whose centers were positioned in a horizontal plane at angles of $\pm 65^\circ$ and $\pm 115^\circ$ with respect to the beam axis at a distance of 22.5 cm (20.5 cm) from the target. The orientation of the clusters was chosen in such a way that three capsules were lined up vertically. An additional single Ge detector was placed at 0°. It seems worth pointing out that this setup is extremely well suited for g factor measurements: most of the Ge crystals are placed, in fact, at positions highly sensitive to the observation of small precessions of the angular correlations, namely, close to $\pm 65^\circ$ and close to the plane perpendicular to the field direction. Furthermore, the full angular correlation is measured simultaneously without the necessity of moving detectors to measure locally the slope of the correlation.

Each cluster detector consists of seven hexagonal tapered Ge crystals of 55%–60% relative efficiency, as indicated in Fig. 1. Only for the central crystal does the center of the crystal face lie on the detector plane, i.e., the horizontal plane containing the beam axis. Consequently, both the angle θ_i, defined as the angle between the beam axis and the projection of the center of the crystal face onto the detector plane, and the out-of-plane angle φ_i have to be considered in the analysis. They can be calculated for each of the 28 individual Ge crystals from the dimensions of the cluster detectors and the target-detector distance. This procedure is discussed in detail in Refs. [12,13], which present g-factor measurements using the recoil distance transient field (RDTF) technique and a very similar cluster detector setup.

III. DATA PREPARATION

For each of the four Si diodes a two-dimensional matrix was sorted with the γ-ray energy detected in the Ge detectors on one axis and the energy of the charged particle registered in the Si detector on the other. Only those events in which the γ-ray and the particle were detected in prompt coincidence were considered. The random background, mainly caused by Rutherford scattered beam particles and γ rays emitted in the deexcitation of the Coulomb excited Gd isotopes from the natural Gd target layer, was carefully subtracted. An example of such a matrix for one of the inner Si diodes and the run with the ^{124}Sn beam is shown in Fig. 2. Interestingly, besides the γ rays belonging to the Coulomb excited ^{124}Sn beam particles observed in coincidence with the C target recoils detected at relatively high energy in the Si detector (region d in Fig. 2), clearly additional particle-γ correlations are observed in three different Si energy bands (regions a–c in Fig. 2).

This observation indicates that, in addition to the Coulomb excitation of the projectile, other competing reactions involving the emission of charged particles are observed. The γ-ray spectra obtained by projecting the matrix of Fig. 2 in the four indicated regions, a–d, are shown in Fig. 3. Inspection of the lines observed in each spectrum reveals that the particles in bands a, b, and c are detected in coincidence with known γ transitions in ^{130}Xe, ^{128}Te, and ^{126}Te, respectively. The more energetic particles of region d correspond to the carbon target ions recoiling from the target after the Coulomb excitation

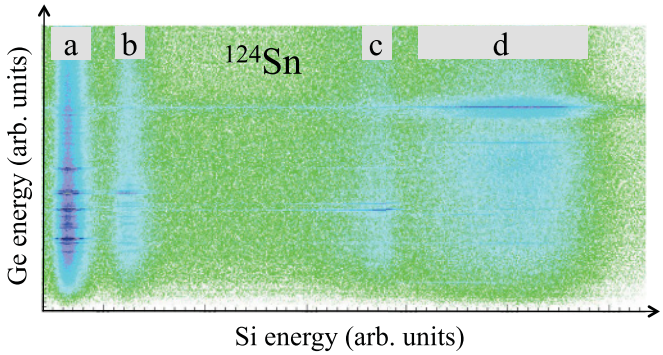

FIG. 2. (Color online) Two-dimensional illustration of the correlation between the energy of the charged particle detected in one of the inner Si diodes and the γ-ray energy detected in the Ge detectors.

of the ^{124}Sn beam. Although with the current setup it is not possible to determine the nature of the detected charged particles, it is most probable that ^{130}Xe is populated in the fusion-evaporation reaction $^{124}\mathrm{Sn} + {}^{12}\mathrm{C} \rightarrow {}^{136}\mathrm{Ba}^* \rightarrow {}^{130}\mathrm{Xe} + \alpha 2n$, with the evaporated α being detected in the Si detector. ^{128}Te is excited via the transfer of an α particle from the ^{12}C target ion to the ^{124}Sn projectile. The remaining ^{8}Be decays nearly instantaneous into two α particles, which are detected in the Si diodes. This α transfer reaction has already previously been successfully employed to measure magnetic moments in unstable nuclei [14]. Finally, the most probable explanation for the observation of γ rays belonging to ^{126}Te [Fig. 3(c)] is the incomplete fusion reaction between the ^{12}C target ion and the ^{124}Sn beam. In this reaction the ^{12}C ion breaks up

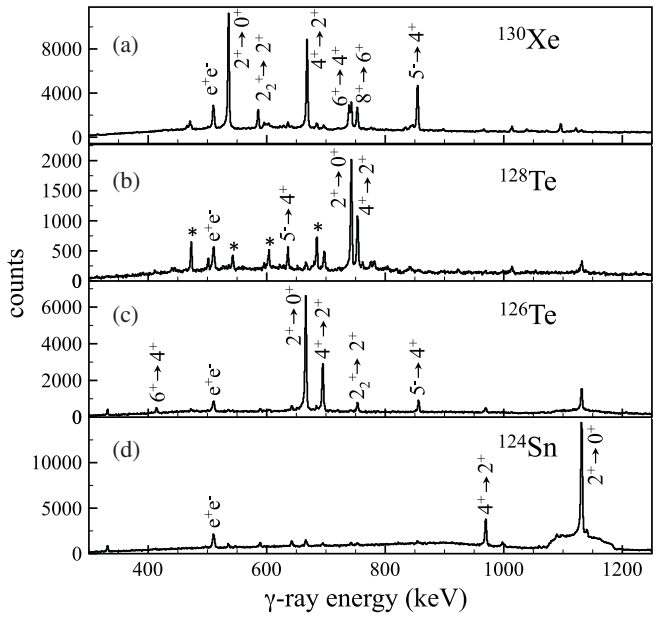

FIG. 3. The γ-ray spectra produced by projection of the matrix shown in Fig. 2 on the ordinate in the ranges a, b, c, and d indicated in Fig. 2. (a) Fusion-evaporation channel $^{124}\mathrm{Sn} + {}^{12}\mathrm{C} \rightarrow {}^{136}\mathrm{Ba}^* \rightarrow {}^{130}\mathrm{Xe} + \alpha 2n$, (b) α transfer channel leading to ^{128}Te, (c) incomplete fusion channel $^{124}\mathrm{Sn} + {}^{8}\mathrm{Be} \rightarrow {}^{132}\mathrm{Xe}^* \rightarrow {}^{126}\mathrm{Te} + \alpha 2n$, and (d) Coulomb excitation channel populating excited states in ^{124}Sn.

into an α particle and ^{8}Be, the ^{8}Be fuses with the ^{124}Sn ion, and ^{126}Te is populated via the $\alpha 2n$ evaporation channel, while the high-energy α particle from the breakup is detected in the particle detector.

IV. DATA ANALYSIS AND RESULTS

A. Angular correlations

For the determination of angular correlation coefficients, the Ge crystals were divided into 13 different groups, according to their angle θ_i with respect to the beam: $\theta_i + 0^\circ$, $\pm 52^\circ$, $\pm 65^\circ$, $\pm 78^\circ$, $\pm 102^\circ$, $\pm 115^\circ$, and $\pm 128^\circ$ ($\theta_i + 0^\circ$, $\pm 51^\circ$, $\pm 65^\circ$, $\pm 79^\circ$, $\pm 101^\circ$, $\pm 115^\circ$, and $\pm 129^\circ$ for the ^{122,124}Sn runs). For each of these 13 groups, two spectra were sorted comprising the γ rays observed in coincidence with the ^{12}C target recoils in either the inner or the outer Si diodes. The two pairs of Si detectors, inner and outer, were treated separately because of the different kinematical conditions. Figure 4 illustrates the relative yields available for all studied Sn isotopes. It shows the sum spectra obtained for the Ge detectors positioned at $\pm 65^\circ$ with respect to the beam in coincidence with the inner pair of Si detectors. Broad gates have been applied on the Si energy (corresponding to region d in Fig. 2) to maximize the number of counts of these spectra. Small contaminations from the incomplete fusion channels (region c) in the heavy isotopes can be accepted since the corresponding lines do not overlap with

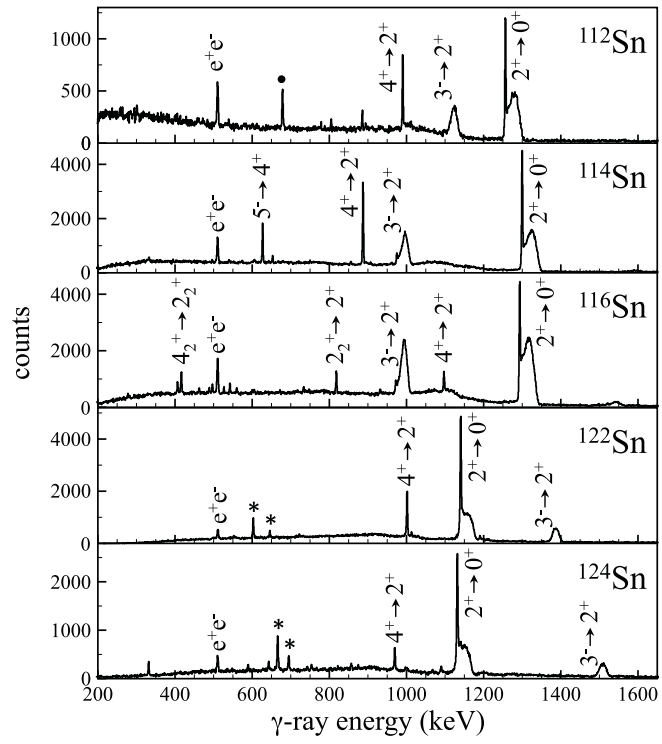

FIG. 4. The γ-ray spectra for ^{112,114,116,122,124}Sn for the Ge detectors positioned at $\pm 65^\circ$ in coincidence with carbon ions detected in the inner pair of Si diodes. Transitions from the α transfer and incomplete fusion channels are labeled by dots and asterisks, respectively.

the lines of interest in the Sn isotopes. In all five isotopes under study both the $2_1^+ \rightarrow 0_1^+$ and the $3_1^- \rightarrow 2_1^+$ transitions show pronounced line shapes, indicating subpicosecond lifetimes for the 2_1^+ and 3_1^- levels. The analysis of these Doppler-shifted line shapes has already been discussed in Ref. [15], and the resulting lifetimes are used for the measurements presented in this work.

For the analysis of the angular correlations, the coordinates θ_i, φ_i are converted into the spherical coordinate system with the polar angle Θ_i and the azimuthal angle Ψ_i. Furthermore, since the short-lived 2_1^+ and 3_1^- states in the studied Sn isotopes decay partially during the passage of the ions through the Gd layer before they are completely stopped in the Cu backing of the multiplayer target, a transformation from the laboratory into the rest frame of the nucleus is required. The formulas used are

$$\cos(\Theta_i') = \frac{\cos(\Theta_i) - \beta}{(1-\beta)\cos(\Theta_i)} \tag{1}$$

and

$$\Psi_i' = \Psi_i, \tag{2}$$

with β being the average velocity of the moving ion at the moment of the emission of the γ ray of interest in units of c, the velocity of light. This average velocity was deduced for each case from the centroid of the line shapes of the $2_1^+ \rightarrow 0_1^+$ and $3_1^- \rightarrow 2_1^+$ transitions. An uncertainty $\Delta\beta = \beta$ has been assumed to account for the velocity distribution reflected by the width of the Doppler-shifted line shapes. In addition to the transformation of the angles, the efficiency-corrected counting rates $W(\Theta_i)$ observed in the Ge detectors positioned at θ_i, φ_i have to be multiplied by the appropriate solid-angle ratio to assure that the γ-ray flux emitted into 4π of solid angle is conserved:

$$W'(\Theta_i') = W(\Theta_i)\frac{[(1-\beta)\cos(\Theta_i)]^2}{1-\beta^2}, \tag{3}$$

where all quantities in the center-of-mass frame are indicated with a prime. The experimental angular correlations obtained for the $2_1^+ \rightarrow 0_1^+$ transitions in ^{112,114,116,122,124}Sn observed in coincidence with C ions detected in the inner and outer pairs of Si detectors are shown in Fig. 5.

The angular correlation coefficients a_2 and a_4 are then determined from a fit of the function $W'(\Theta') = a_0[1 + a_2 P_2(\cos\Theta') + a_4 P_4(\cos\Theta')]$ to the data, where a_0 is a normalization factor. All determined angular correlation coefficients are summarized in Table I. For the $3_1^- \rightarrow 2_1^+$ and $4_1^+ \rightarrow 2_1^+$ transitions the available statistics are much worse. Rather than attempting to determine correlation parameters for each individual case as discussed above for the $2_1^+ \rightarrow 0_1^+$ transition, the angular correlations that exhibit reasonable statistics were fitted all together, as shown in Fig. 6, leading to average coefficients that have then been employed for all isotopes in the determination of the precession angles as discussed below. Since the angular correlations are expected to be quite similar for all cases under study, this approach seems to be justified. From the fitted normalization factors a_0, the feeding intensities of the $3_1^- \rightarrow 2_1^+$ and $4_1^+ \rightarrow 2_1^+$ transitions are determined and listed in Table I.

For the determination of g factors, the logarithmic slope $S'(\theta_i', \varphi_i')$ of the angular correlation in a plane perpendicular to the magnetic field direction is needed:

$$S(\theta_i', \varphi_i') = \frac{1}{W'(\theta_i', \varphi_i')}\frac{dW'(\theta', \varphi_i')}{d\theta'}\bigg|_{\theta_i'}, \tag{4}$$

with θ_i' and φ_i' being the angle with respect to the beam axis in the detector plane and the out-of-plane angle in the rest frame of the nucleus, respectively. The detector positions θ_i' and φ_i' in this reference system are obtained from the spherical coordinates Θ_i' and Ψ_i' defined in Eqs. (1) and (2). Since $S(\theta_i', \varphi_i')$ depends on the out-of-plane angle φ_i' of the Ge crystal, while in the analysis we combined crystals with different values of φ_i for $\theta_i = 65°, 115°$, we have to estimate the systematic error introduced by this procedure. For the correlation coefficients listed in Table I the difference between $S(65°, 0°)$ and $S(65°, 15°)$ is of the order of 1%. The use of an average value of φ_i therefore leads to a negligible contribution to the experimental uncertainties.

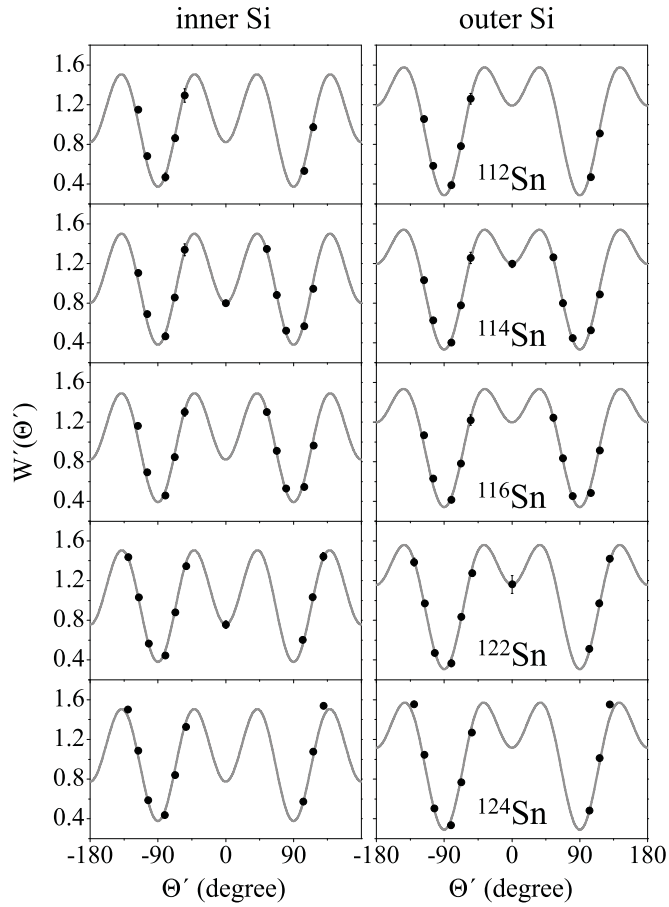

FIG. 5. Experimental angular correlation functions for the $2_1^+ \rightarrow 0_1^+$ transitions in ^{112,114,116,122,124}Sn observed in coincidence with C ions detected in the (left) inner and (right) outer pairs of Si detectors. Both experimental data and fits are normalized to $a_0 = 1$ to facilitate the comparison.

TABLE I. Angular correlation coefficients a_2 and a_4 determined for the inner and outer pairs of Si detectors, respectively, for the $2_1^+ \to 0_1^+$ transition in ^{112,114,116,122,124}Sn. $I^{3^-\to 2^+}$ and $I^{4^+\to 2^+}$ are the intensities of the $3_1^- \to 2_1^+$ and $4_1^+ \to 2_1^+$ feeding transitions relative to that of the $2_1^+ \to 0_1^+$ transition.

Nucleus	E_γ (keV)	Inner Si				Outer Si			
		a_2	a_4	$I^{3^-\to 2^+}$ (%)	$I^{4^+\to 2^+}$ (%)	a_2	a_4	$I^{3^-\to 2^+}$ (%)	$I^{4^+\to 2^+}$(%)
^{112}Sn	1257	0.640(75)	−0.818(82)	24.6(10)	10.7(5)	0.896(55)	−0.706(63)	17.4(6)	7.7(3)
^{114}Sn	1300	0.622(44)	−0.819(48)	26.8(8)	12.2(4)	0.846(37)	−0.650(41)	20.2(7)	9.8(2)
^{116}Sn	1294	0.617(55)	−0.795(60)	29.7(1)	2.2(1)	0.835(46)	−0.638(51)	21.7(7)	1.7(1)
^{122}Sn	1141	0.605(30)	−0.848(31)	17.4(5)	11.1(2)	0.859(29)	−0.702(29)	7.9(7)	5.5(2)
^{124}Sn	1132	0.615(47)	−0.841(52)	17.2(6)	4.8(1)	0.862(60)	−0.746(67)	7.8(4)	2.2(1)

B. Precession angles

In a conventional two-detector g-factor experiment, the precession angles are deduced from the double-counting ratios

$$\rho_\theta = \sqrt{\frac{N^\uparrow(+\theta)}{N^\downarrow(+\theta)}\frac{N^\downarrow(-\theta)}{N^\uparrow(-\theta)}}, \tag{5}$$

where $N^{\uparrow,\downarrow}(\pm\theta)$ are the peak areas of the relevant γ transitions observed in a pair of detectors positioned at $\pm\theta$ for the field directions "up" and "down." The values ρ_θ are defined in such a way that they only depend on peak areas and are independent of other experimental factors, such as detector efficiencies and integral beam currents for the two field directions. In our multidetector experiment, equivalent ρ_{θ_i} values are defined as

$$\rho_{\theta_i} = \left(\prod_{j=1,2}\frac{N_j^\uparrow(+\theta_i)}{N_j^\downarrow(+\theta_i)}\frac{N_j^\downarrow(-\theta_i)}{N_j^\uparrow(-\theta_i)}\right)^{1/4} \tag{6}$$

for $\theta_i = 52^\circ, 78^\circ, 102^\circ, 128^\circ$ and

$$\rho_{\theta_i} = \left(\prod_{j=1-3}\frac{N_j^\uparrow(+\theta_i)}{N_j^\downarrow(+\theta_i)}\frac{N_j^\downarrow(-\theta_i)}{N_j^\uparrow(-\theta_i)}\right)^{1/6} \tag{7}$$

for $\theta_i = 65^\circ, 115^\circ$. These geometrical means of four and six individual counting rate ratios constitute the natural extension of Eq. (5) to our multidetector setup.

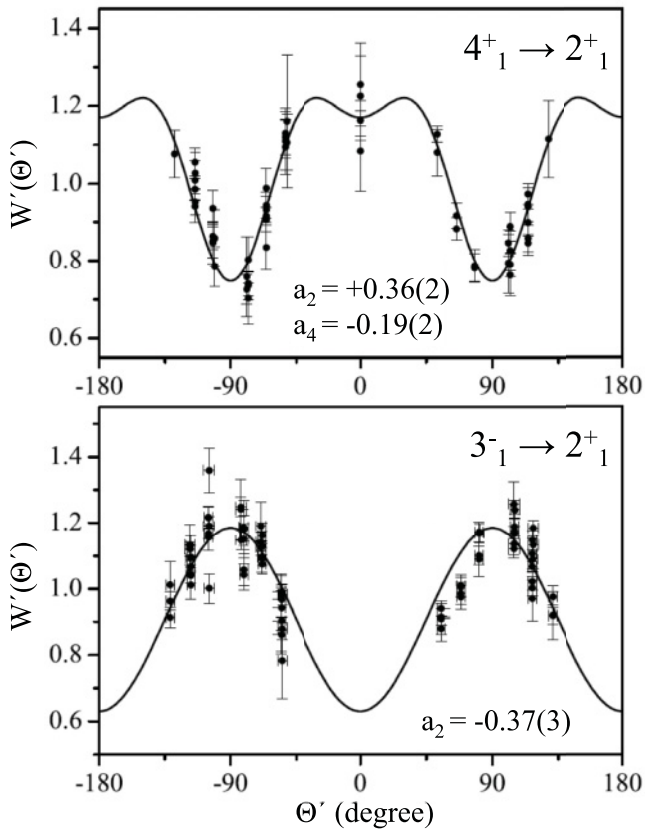

FIG. 6. Experimental angular correlation functions for the (top) $4_1^+ \to 2_1^+$ and (bottom) $3_1^- \to 2_1^+$ transitions in a number of Sn isotopes and either pair of Si detectors. The solid lines are the fits to the data points resulting in the angular correlation coefficients given. For the $3_1^- \to 2_1^+$ transition $a_4 = 0$ has been fixed in the fit.

At this point, usully the so-called symmetric double ratios are defined and investigated as well, which combine the counting rates in pairs of detectors positioned at angles differing by 180° with respect to the beam axis (see, for example, Ref. [12]). These ratios are identical to one per definition and provide, in general, an excellent criterion as to the quality of the data, and they help to reveal inherent systematic uncertainties. However, in the present experiments, due to the large velocities of the moving ions at the moment of the γ-ray emission, the slope values are significantly different in the forward and backward directions. For a pair of detectors positioned at + 65° and −115° in the laboratory frame, the slopes differ by typically 10%–20% for the $2^+ \to 0^+$ transition and 20%–25% for the $3^- \to 2^+$ transition (compare Tables II and IV). Consequently, the symmetric double ratios do not have to be identical to 1 in our case and therefore, unfortunately, cannot be used as a consistency check of the data.

The measured effect ϵ_{θ_i} for each γ transition of interest and each of the six values ρ_{θ_i} can be expressed as

$$\epsilon_{\theta_i} = \frac{\rho_{\theta_i} - 1}{\rho_{\theta_i} + 1}. \tag{8}$$

Finally, the precession angles

$$\Delta\Phi_{\theta_i} = \epsilon_{\theta_i}/S(\theta_i', \varphi_i') \tag{9}$$

are calculated from the measured effects and logarithmic slopes. In Tables II–IV, the values of ρ_{θ_i}, the logarithmic slopes $S(\theta_i', \varphi_i')$, and the precession angles $\Delta\Phi_{\theta_i}$ are summarized for the $2_1^+ \to 0_1^+$, the $4_1^+ \to 2_1^+$, and the $3_1^- \to 2_1^+$ transitions, respectively. For the latter two transitions, the precession

TABLE II. Precessions $\Delta\Phi^{20}_{\theta_i}$ deduced from the γ-ray spectra obtained in coincidence with C ions detected in the inner and outer pairs of Si detectors for the $2^+_1 \rightarrow 0^+_1$ transition in ^{112,114,116,122,124}Sn. For each transition, the detector angle in the rest frame θ'_i, ρ_{θ_i}, the logarithmic slope $S(\theta'_i,\varphi'_i)$, and the precession angle $\Delta\Phi^{20}_{\theta_i}$ are listed. The mean precession angles $\Delta\Phi^{20}_{\text{ave}}$ are also given.

Inner Si					Outer Si				
θ'_i(deg)	ρ_{θ_i}	$S(\theta'_i,\varphi'_i)$	$\Delta\Phi^{20}_{\theta_i}$ (mrad)	$\Delta\Phi^{20}_{\text{ave}}$ (mrad)	θ'_i(deg)	ρ_{θ_i}	$S(\theta'_i,\varphi'_i)$	$\Delta\Phi^{20}_{\theta_i}$ (mrad)	$\Delta\Phi^{20}_{\text{ave}}$ (mrad)
				^{112}Sn					
54.0	0.997(18)	−1.120(95)	1.2(82)		54.3	1.016(11)	−1.403(76)	−5.8(38)	
67.0	1.034(19)	−2.323(189)	−7.2(40)		67.4	1.020(11)	−2.686(163)	−3.6(20)	
79.9	1.022(34)	−2.632(303)	−4.2(63)	-3.7 ± 2.4	80.3	1.061(21)	−3.147(311)	−9.3(32)	-5.4 ± 1.3
104.3	1.017(28)	2.813(274)	3.0(50)		104.7	0.966(16)	3.293(250)	−5.3(26)	
117.0	0.967(24)	1.972(157)	−8.6(64)		117.3	0.974(14)	2.215(127)	−5.9(33)	
				^{114}Sn					
54.0	1.007(8)	−1.103(56)	−3.3(36)		54.3	1.030(13)	−1.338(51)	−10.9(49)	
67.0	1.007(8)	−2.295(110)	−1.4(18)		67.4	0.988(14)	−2.469(105)	2.4(29)	
79.9	1.016(15)	−2.572(173)	−3.2(29)	-1.7 ± 1.1	80.3	0.976(30)	−2.666(170)	4.5(57)	-0.2 ± 2.4
104.3	0.989(13)	2.761(158)	−2.1(23)		104.7	0.988(22)	2.902(150)	−2.1(38)	
117.0	1.003(12)	1.945(91)	0.7(31)		117.3	1.010(20)	2.069(83)	2.4(48)	
				^{116}Sn					
54.1	1.001(8)	−1.100(70)	−0.6(38)		54.3	0.995(12)	−1.323(64)	1.7(45)	
67.1	0.994(8)	−2.250(138)	1.2(18)		67.4	1.008(12)	−2.423(130)	−1.5(25)	
80.0	1.013(15)	−2.457(208)	−2.6(29)	-0.7 ± 1.3	80.3	0.990(23)	−2.572(204)	1.9(45)	$+0.1 \pm 1.6$
104.4	0.975(12)	2.670(192)	−4.7(24)		104.7	0.997(19)	2.823(182)	−0.6(34)	
117.1	1.009(12)	1.900(114)	2.3(31)		117.3	1.010(17)	2.038(103)	2.4(41)	
				^{122}Sn					
52.1	0.983(13)	−0.920(34)	9.5(70)		52.4	1.005(26)	−1.196(35)	−2.1(106)	
66.2	0.990(13)	−2.235(69)	2.3(29)		66.5	1.049(28)	−2.514(74)	−9.5(53)	
80.2	0.951(24)	−2.592(115)	9.7(49)	$+5.2 \pm 1.8$	80.5	0.965(59)	−2.923(141)	6.0(104)	$+2.0 \pm 4.9$
102.3	1.031(22)	2.768(111)	5.5(39)		102.7	1.132(57)	3.139(128)	19.7(80)	
116.1	1.017(19)	2.028(62)	4.2(46)		116.5	1.037(39)	2.231(63)	8.1(83)	
129.9	1.017(13)	0.742(32)	11.4(85)		130.2	1.017(25)	0.979(32)	8.4(124)	
				^{124}Sn					
52.6	1.009(12)	−0.975(55)	−4.4(60)		52.6	0.972(15)	−1.222(74)	11.9(62)	
66.7	0.970(12)	−2.291(117)	6.6(27)		66.8	0.970(16)	−2.625(167)	5.9(32)	
80.8	0.951(23)	−2.529(189)	9.9(49)	$+5.6 \pm 1.8$	80.8	0.900(37)	−3.113(336)	16.9(68)	$+8.1 \pm 1.9$
102.9	1.013(19)	2.794(179)	2.3(34)		103.0	1.035(29)	3.343(292)	5.1(42)	
116.7	1.028(17)	1.984(99)	7.0(41)		116.8	1.045(22)	2.262(138)	9.8(46)	
130.4	1.019(11)	0.709(49)	13.3(77)		130.4	1.014(13)	0.953(65)	7.4(67)	

analysis could only be performed for the cases in which they were observed with sufficient statistics. Tables II–IV also include the weighted-mean values of the precession angles obtained for the different angle groups. It should be noted that in the case of the $2^+_1 \rightarrow 0^+_1$ transition the values cannot be inferred *a priori* to be the same due to the different feeding from the 3^-_1 and 4^+_1 states.

C. *g* factors

For the 4^+_1 and 3^-_1 states, the g factors can now be deduced directly from the measured precessions summarized in Tables III and IV, using the calculated transient field precessions per unit g factor, which are given by

$$\phi(\tau) = \Delta\Phi/g = -\frac{\mu_N}{\hbar}\int_{t_{\text{in}}}^{t_{\text{out}}} B_{\text{TF}}(t)e^{-t/\tau}dt, \qquad (10)$$

where τ is the lifetime of the excited state under study and t_{in} and t_{out} are the times when the recoiling nuclei enter and leave the ferromagnetic Gd target layer, respectively. For the parametrization of the transient field strength, we adopted the linear parametrization [16]

$$B_{\text{TF}}[v(t), Z] = GaZ(v/v_0), \qquad (11)$$

where a is the field parameter, which, in the case of a gadolinium target, is 17 T, Z is the atomic number of the recoiling ion, v/v_0 is the velocity of the ion in units of the Bohr velocity, and G is an attenuation factor that takes into account the beam-induced reduction of the transient field strength. G depends on the average energy loss of the ions in the ferromagnetic layer [16], and for the present experimental conditions a value of $G = 0.55(5)$ has been adopted. Using Eqs. (10) and (11), the integral precessions have been calculated for the 2^+_1, 4^+_1, and 3^-_1, states taking into account their lifetimes and the time-dependent strength of the transient field during the passage of the excited nuclei through the ferromagnetic layer. The resulting values ϕ_{20}, ϕ_{42},

TABLE III. Precessions $\Delta\Phi^{42}_{\theta_i}$ deduced from the γ-ray spectra obtained in coincidence with C ions detected in the inner and outer pairs of Si detectors for the $4^+_1 \rightarrow 2^+_1$ transition in ^{112,114,116,122}Sn. For each transition, the detector angle in the rest frame θ'_i, ρ_{θ_i}, the logarithmic slope $S(\theta'_i,\varphi'_i)$, and the precession angle $\Delta\Phi^{42}_{\theta_i}$ are listed. The mean precession angles $\Delta\Phi^{42}_{\text{ave}}$ are also given.

Inner Si					Outer Si				
θ'_i(deg)	ρ_{θ_i}	$S(\theta'_i,\varphi'_i)$	$\Delta\Phi^{42}_{\theta_i}$ (mrad)	$\Delta\Phi^{42}_{\text{ave}}$ (mrad)	θ'_i(deg)	ρ_{θ_i}	$S(\theta'_i,\varphi'_i)$	$\Delta\Phi^{42}_{\theta_i}$ (mrad)	$\Delta\Phi^{42}_{\text{ave}}$ (mrad)
				^{112}Sn					
52.2	1.006(87)	−0.554(28)	−5(78)		52.2	0.903(62)	−0.554(28)	92(62)	
65.0	1.129(93)	−0.762(43)	−79(54)		65.0	1.076(57)	−0.762(43)	−48(35)	
77.8	1.263(140)	−0.598(38)	−194(92)	-68 ± 32	77.8	1.164(81)	−0.598(38)	−127(58)	-26 ± 30
102.2	1.026(93)	0.598(38)	22(75)		102.2	1.014(63)	0.598(38)	11(52)	
115.0	0.854(92)	0.762(43)	−104(70)	^{112}Sn	115.0	0.972(76)	0.762(43)	−19(51)	
				^{114}Sn					
52.2	1.011(27)	−0.554(28)	−10(24)		52.2	0.953(48)	−0.554(28)	44(46)	
65.0	1.000(25)	−0.762(43)	0(16)		65.0	1.023(46)	−0.762(43)	−15(30)	
77.8	1.019(34)	−0.598(38)	−16(28)	-9 ± 10	77.8	1.098(68)	−0.598(38)	−78(52)	-24 ± 20
102.2	0.945(29)	0.598(38)	−48(26)		102.2	0.912(56)	0.598(38)	−77(51)	
115.0	1.024(39)	0.762(43)	15(25)		115.0	0.951(67)	0.762(43)	−33(46)	
				^{116}Sn					
52.2	0.964(149)	−0.554(28)	33(140)		52.2	0.734(243)	−0.554(28)	276(292)	
65.0	1.018(112)	−0.762(43)	−12(72)		65.0	0.858(206)	−0.762(43)	100(157)	
77.8	1.029(131)	−0.598(38)	−24(107)	-20 ± 47	77.8	0.972(211)	−0.598(38)	24(182)	$+76 \pm 89$
102.2	0.790(136)	0.598(38)	−196(143)		102.2	0.963(223)	0.598(38)	−32(194)	
115.0	1.074(195)	0.762(43)	47(119)		115.0	1.238(455)	0.762(43)	140(238)	
				^{122}Sn					
51.1	0.957(46)	−0.527(27)	41(46)		51.1	0.734(243)	−0.527(27)	−151(187)	
65.0	0.925(39)	−0.760(43)	51(28)		65.0	0.858(206)	−0.760(43)	46(108)	
78.9	0.909(52)	−0.556(36)	86(51)	$+22 \pm 20$	78.9	0.972(211)	−0.556(36)	169(180)	$+3 \pm 58$
101.1	1.025(53)	0.556(36)	22(47)		101.1	0.963(223)	0.556(36)	−116(169)	
115.0	0.985(58)	0.760(43)	−10(39)		115.0	1.238(455)	0.760(43)	−58(123)	
128.9	0.931(42)	0.527(27)	−68(43)		128.9	1.238(455)	0.527(27)	73(136)	

and ϕ_{32} are listed for all Sn isotopes under study in Table V together with the corresponding lifetimes employed in the calculation. Finally, the experimental g factors obtained for the 4^+_1 and 3^-_1 states are listed in Table VI and illustrated in Fig. 7. Note that in the case of the 4^+_1 state in ^{114}Sn, the g factor deduced from the observed precession of the $4^+_1 \rightarrow 2^+_1$ transition has to be considered as an effective value given the significant feeding of the 4^+_1 from a 5^-_1 level (compare with Fig. 4).

For the first excited 2^+ states the determination of the g factors unfortunately is not as straightforward as discussed above for the 4^+_1 and 3^-_1 states. The spectra shown in Fig. 4 clearly indicate that, besides their direct excitation, the 2^+_1 states in the Sn isotopes in the current experiment are also fed from higher-lying states, in particular the 3^-_1 and 4^+_1 levels. The observed intensities of the $3^-_1 \rightarrow 2^+_1$ and $4^+_1 \rightarrow 2^+_1$ transitions amount to up to 30% and 12% of the intensity, respectively, of the $2^+_1 \rightarrow 0^+_1$ ground-state transition (compare Table I). Consequently, the contribution of these feeding transitions to the observed precession of the angular correlation of the $2^+_1 \rightarrow 0^+_1$ transition has to be evaluated before the g factor of the 2^+_1 state can be deduced from the measured precession angles. The general prescription for these feeding corrections has been given, for example, in Refs. [18,19]. For the simple case of only two directly populating transitions the formula given in [18,19] can be simplified to

$$g(2^+_1)_{\theta_i} = \frac{\frac{dW'_{\text{obs}}}{d\theta'}\big|_{\theta'_i}(1+\eta_{32}+\eta_{42})\Delta\Phi^{20}_{\theta_i} - \eta_{32}\frac{dW'_{320}}{d\theta'}\big|_{\theta'_i}\Delta\Phi^{32}_{\text{ave}} - \eta_{42}\frac{dW'_{420}}{d\theta'}\big|_{\theta'_i}\Delta\Phi^{42}_{\text{ave}}}{\frac{dW'_{20}}{d\theta'}\big|_{\theta'_i}\phi_{20} + \eta_{32}\frac{dW'_{320}}{d\theta'}\big|_{\theta'_i}\phi_{320} + \eta_{42}\frac{dW'_{420}}{d\theta'}\big|_{\theta'_i}\phi_{420}}, \tag{12}$$

where η_{32} and η_{42} are the excitation cross sections of the 3^-_1 and 4^+_1 states relative to the direct excitation of the 2^+_1 state, which in the present work are deduced from the observed intensities of the $2^+_1 \rightarrow 0^+_1$, $3^-_1 \rightarrow 2^+_1$, and $4^+_1 \rightarrow 2^+_1$ transitions (see Table I). W'_{obs} is the observed angular correlation of the $2^+_1 \rightarrow 0^+_1$ transition, while W'_{20}, W'_{320}, and W'_{420} are the angular

TABLE IV. Precessions $\Delta\Phi^{32}_{\theta_i}$ deduced from the γ-ray spectra obtained in coincidence with C ions detected in the inner and outer pairs of Si detectors for the $3^-_1 \rightarrow 2^+_1$ transition in ^{112,114,116}Sn. For each transition, the detector angle in the rest frame θ'_i, ρ_{θ_i}, the logarithmic slope $S(\theta'_i,\varphi'_i)$, and the precession angle $\Delta\Phi^{32}_{\theta_i}$ are listed. The mean precession angles $\Delta\Phi^{32}_{\text{ave}}$ are also given.

Inner Si					Outer Si				
θ'_i (deg)	ρ_{θ_i}	$S(\theta'_i,\varphi'_i)$	$\Delta\Phi^{32}_{\theta_i}$ (mrad)	$\Delta\Phi^{32}_{\text{ave}}$ (mrad)	θ'_i (deg)	ρ_{θ_i}	$S(\theta'_i,\varphi'_i)$	$\Delta\Phi^{32}_{\theta_i}$ (mrad)	$\Delta\Phi^{32}_{\text{ave}}$ (mrad)
				^{112}Sn					
54.8	0.860(92)	0.512(42)	−147(105)		54.8	1.102(71)	0.512(42)	94(63)	
67.9	1.033(49)	0.338(32)	48(70)		67.9	1.057(35)	0.338(32)	82(50)	
80.9	0.980(45)	0.146(15)	−71(159)	−41 ± 44	80.9	1.004(32)	0.146(15)	14(109)	+47 ± 29
105.3	1.034(50)	−0.242(24)	−70(100)		105.3	0.994(33)	−0.242(24)	12(68)	
117.9	1.079(94)	−0.417(37)	−91(105)		117.9	1.024(60)	−0.417(37)	−28(70)	
				^{114}Sn					
54.7	1.028(32)	0.513(42)	26(30)		54.7	1.018(71)	0.513(42)	17(68)	
67.9	1.041(20)	0.340(32)	59(29)		67.9	1.004(41)	0.340(32)	6(60)	
80.8	1.019(20)	0.147(15)	65(68)	+34 ± 16	80.8	0.977(40)	0.147(15)	−80(140)	+19 ± 34
105.2	1.006(19)	−0.241(24)	−12(39)		105.2	0.987(39)	−0.241(24)	28(81)	
117.8	0.970(33)	−0.416(37)	37(41)		117.8	0.945(63)	−0.416(37)	69(80)	
				^{116}Sn					
54.8	1.006(29)	0.512(42)	6(28)		54.8	0.999(57)	0.512(42)	−1(55)	
67.9	0.983(18)	0.338(32)	−26(28)		67.9	0.934(33)	0.338(32)	−102(53)	
80.9	0.996(18)	0.146(15)	−15(63)	+3 ± 15	80.9	0.982(33)	0.146(15)	−63(117)	−12 ± 36
105.3	0.985(19)	−0.242(24)	30(40)		105.3	0.946(33)	−0.242(24)	114(72)	
117.9	0.976(29)	−0.417(37)	29(36)		117.9	0.986(52)	−0.417(37)	17(63)	

TABLE V. Calculated integral precession angles ϕ_{20}, ϕ_{32}, and ϕ_{42} for the $2^+_1 \rightarrow 0^+_1$, $3^-_1 \rightarrow 2^+_1$, and $4^+_1 \rightarrow 2^+_1$ transitions [calculated using Eq. (10)] and for the $2^+_1 \rightarrow 0^+_1$ transition after population of the 2^+_1 state from the 3^-_1 and 4^+_1 levels, ϕ_{320} and ϕ_{420}, respectively [calculated using Eq. (13)] for $g = 1$ and $G = 0.55(5)$.

	τ (ps)[a]							
Nucleus	2^+_1	3^-_1	4^+_1	$-\phi_{20}$ (mrad)	$-\phi_{32}$ (mrad)	$-\phi_{42}$(mrad)	$-\phi_{320}$ (mrad)	$-\phi_{420}$ (mrad)
^{112}Sn	0.65(4)	0.31(2)	4.8(9)	72(7)	43(4)	122(12)	56(6)	8(1)
^{114}Sn	0.60(4)	0.52(3)	7.6(6)	69(7)	64(6)	126(13)	43(4)	5(1)
^{116}Sn	0.67(4)	0.48(3)	4.0[b]	74(7)	61(6)	120(12)	46(5)	9(1)
^{122}Sn	1.29(8)	0.13(2)	2.3(3)	97(10)	17(2)	111(10)	90(9)	19(2)
^{124}Sn	1.48(15)	0.10(1)	5.3(7)	96(10)	11(1)	112(11)	90(9)	11(1)

[a]Taken from Refs. [15,17]

[b]Value adopted in the calculation of the integral precession since the literature values $\tau = 0.4(2)$ ps and $\tau = 0.68(13)$ ps [17] are in disagreement with the observed line shape of the $4^+_1 \rightarrow 2^+_1$ transition.

TABLE VI. g factors of the 2^+_1, 4^+_1, and 3^-_1 states in ^{112,114,116,122,124}Sn.

	$g(2^+_1)$			$g(4^+_1)$			$g(3^-_1)$		
Nucleus	Inner Si	Outer Si	Average	Inner Si	Outer Si	Average	Inner Si	Outer Si	Average
^{112}Sn	+0.084(65)	+0.112(41)	+0.104(35)	+0.56(26)	+0.21(25)	+0.38(18)	+0.97(104)	−1.07(66)	−0.48(92)
^{114}Sn	+0.131(32)	+0.079(39)	+0.110(25)	+0.07(8)[a]	+0.19(16)[a]	+0.09(7)[a]	−0.54(26)	−0.29(52)	−0.49(23)
^{116}Sn	+0.015(27)	−0.003(27)	+0.006(19)	+0.17(39)	−0.63(74)	0.00(35)	−0.05(25)	+0.19(58)	−0.01(23)
^{122}Sn	−0.048(20)	−0.017(50)	−0.044(19)	−0.20(18)	−0.03(52)	−0.18(17)	···	···	0.0(5)[b]
^{124}Sn	−0.055(18)	−0.083(21)	−0.067(14)	···	···	0.0(5)[b]	···	···	0.0(5)[b]

[a]Effective value due to the observed feeding from a 5^- level into the 4^+_1 state.

[b]Value adopted in the feeding correction for the 2^+_1 states.

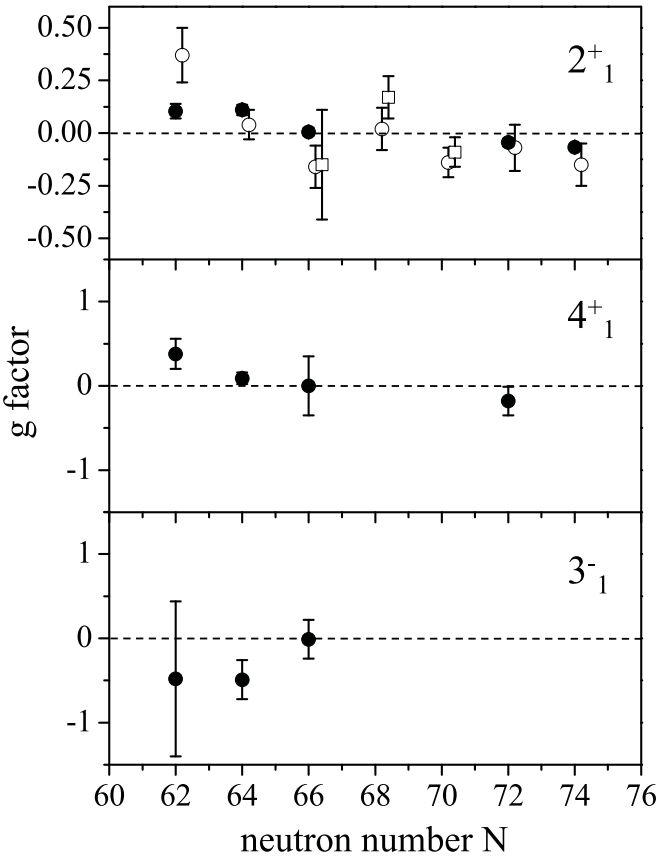

FIG. 7. Experimental g factors of the (top) 2^+_1, (middle) 4^+_1, and (bottom) 3^-_1 states in Sn isotopes from the present work (solid circles) compared to literature values (open circles: Ref. [10]; open squares: Ref. [11]).

correlations of the same transition corresponding either to direct population of the 2^+_1 state or to indirect population via feeding from the 3^-_1 or 4^+_1 state. $\Delta\Phi^{20}_{\theta_i}$, $\Delta\Phi^{32}_{\rm ave}$, and $\Delta\Phi^{42}_{\rm ave}$ are the precessions of the $2^+_1 \rightarrow 0^+_1$ transition observed in the detectors positioned at angle θ_i with respect to the beam and the average precessions of the $3^-_1 \rightarrow 2^+_1$ and $4^+_1 \rightarrow 2^+_1$ transitions, respectively. ϕ_{20} is the integral precession per unit g factor of the $2^+_1 \rightarrow 0^+_1$ transition after direct population of the 2^+_1 state, while ϕ_{320} and ϕ_{420} are the corresponding values in case of the feeding of the 2^+_1 state from the 3^-_1 and 4^+_1 states. The latter are calculated as

$$\phi_{320} = -\frac{\mu_N}{\hbar}\int_{t_{\rm in}}^{t_{\rm out}} \frac{\tau(2^+)}{\tau(3^-)-\tau(2^+)} \times (e^{-t/\tau(3^-)} - e^{-t/\tau(2^+)})B_{\rm TF}(t)dt \qquad (13)$$

(and analogously for ϕ_{420}) and are included in Table V.

The slope of the angular correlation of the observed $2^+_1 \rightarrow 0^+_1$ transition, $dW'_{\rm obs}/d\theta'$, is calculated for each group of detectors positioned at θ_i from the a_2 and a_4 coefficients listed in Table I. For W'_{320} the parameters $a_2 = 0.57(3), a_4 = -0.57(3)$ are employed since the experimentally observed angular correlations of the $3^-_1 \rightarrow 2^+_1$ transitions shown in Fig. 6 are in agreement within the experimental uncertainties with the maximum alignment parameters $a_2 = -0.4$, $a_4 = 0$. For the

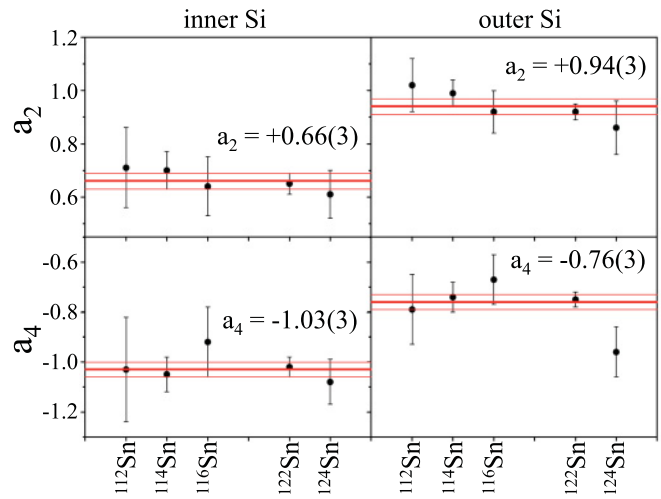

FIG. 8. (Color online) Angular correlation coefficients for the $2^+_1 \rightarrow 0^+_1$ transition after direct population of the 2^+_1 state obtained from a fit of the observed $2^+_1 \rightarrow 0^+_1$ angular correlations as described in the text.

case of the feeding from the 4^+_1 state, W'_{420} is identical to W'_{42}, so that the experimentally obtained parameters $a_2 = 0.36(2)$, $a_4 = -0.19(2)$ (see Fig. 6) are used to calculate the slopes $dW'_{420}/d\theta'$.

The angular correlation of the $2^+_1 \rightarrow 0^+_1$ transition after direct population of the 2^+_1 state, W'_{20}, has been extracted from the observed correlation $W'_{\rm obs}$ and the known feeding intensities (see Table I) using the relation

$$W'_{\rm obs}(\Theta') = (1 - I^{4^+\rightarrow 2^+} - I^{3^-\rightarrow 2^+})W'_{20}(\Theta') + I^{4^+\rightarrow 2^+}W'_{420}(\Theta') + I^{3^-\rightarrow 2^+}W'_{320}(\Theta'). \qquad (14)$$

This fit has been performed for all ten angular correlations $W'_{\rm obs}(\Theta')$ shown in Fig. 5, and the resulting coefficients a_2 and a_4 of $W'_{20}(\Theta')$ are plotted for all Sn isotopes under study in Fig. 8. As can be seen from Fig. 8, this fitting procedure yields quite consistent numbers, and therefore average coefficients have then been employed in the calculation of 2^+_1 g factors corrected for feeding using Eq. (12).

For the 4^+_1 states in ^{112,114,116,122}Sn and the 3^-_1 states in ^{112,114,116}Sn the experimentally determined average precessions $\Delta\Phi^{42}_{\rm ave}$ and $\Delta\Phi^{32}_{\rm ave}$ (see Tables III and IV) have been employed in the calculation of $g(2^+_1)_{\theta_i}$ using Eq. (12). For the 4^+_1 and 3^-_1 levels in ^{124}Sn as well as the 3^-_1 state in ^{122}Sn, g factors of $g = 0.0(5)$ have been assumed, and the corresponding precessions $\Delta\Phi^{42}$ and $\Delta\Phi^{32}$ have been deduced from the ϕ_{42} and ϕ_{32} values listed in Table V. However, this assumption does not have a strong impact on the deduced $g(2^+_1)$ since, first, the intensity of the $4^+_1 \rightarrow 2^+_1$ feeding transition in ^{124}Sn is small and, second, the integral precessions ϕ_{32} are small for ^{122,124}Sn because of the short lifetimes of the 3^-_1 states in these two isotopes. Finally, the resulting g factor $g(2^+_1)$ is deduced as the weighted mean of the values $g(2^+_1)_{\theta_i}$ obtained for the individual detector groups. The feeding-corrected g factors of the 2^+_1 states in ^{112,114,116,122,124}Sn are included in Table VI and illustrated in Fig. 7.

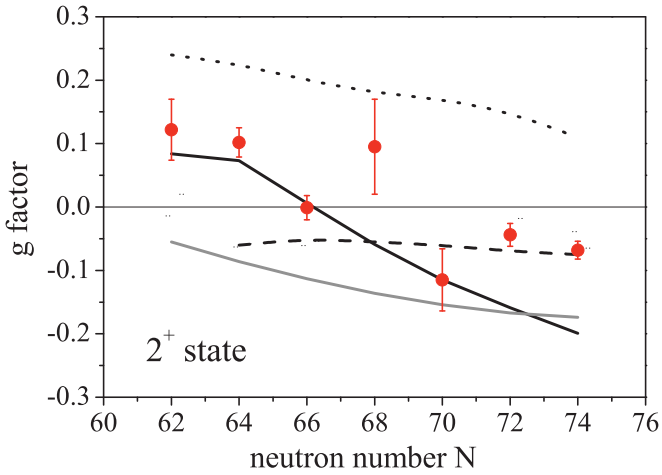

FIG. 9. (Color online) Adopted experimental g factors of 2_1^+ states in stable Sn isotopes compared to RQRPA (dotted line) [26,27], QRPA (dashed line) [28], and shell-model calculations using a ^{100}Sn core (solid black line) or a ^{132}Sn core (grey line). See text for details.

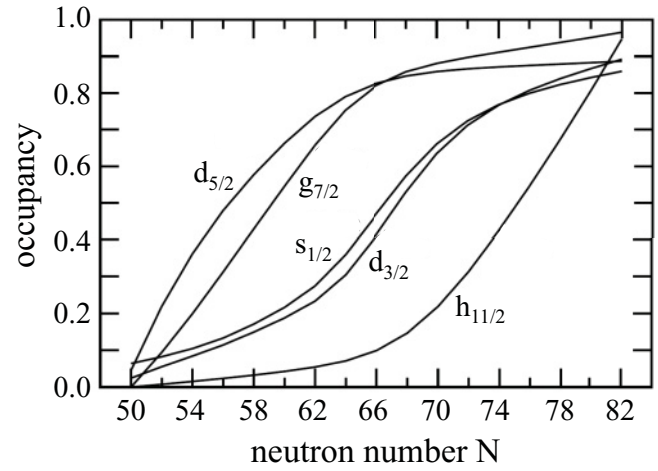

FIG. 10. Occupancies of the neutron single-particle orbitals between $N = 50$ and $N = 82$ as a function of the mass number (adopted from Ref. [20]).

Before closing this section we consider it worth mentioning that due to the small absolute values of $g(2_1^+)$ the dependence of the results on the choice of the transient field parametrization adopted in the analysis is rather limited and does not affect significantly the following discussion and interpretation. To give one example, in the case of the 2^+ state in ^{124}Sn, for which the largest precession angle was measured, the use of the parametrization employed in Ref. [11] instead of Eq. (11) increases the absolute value of $g(2_1^+)$ by 0.02.

V. DISCUSSION AND INTERPRETATION

We will now discuss the experimentally obtained excited state g factors in the stable semi-magic Sn isotopes first in a qualitative way and then on the basis of results of large-scale shell-model calculations. For the 2_1^+ states, adopted experimental g factors are considered (weighted-mean values of the results obtained in the present work and in Refs. [10,11]) and are shown in Fig. 9.

A. Qualitative discussion of the results

For a qualitative understanding of the results we combine the information concerning the occupancies of the neutron single-particle orbitals in the major $N = 50$–82 shell with the known empirical g factors of these orbitals. The occupancies of the neutron single-particle orbitals in the ground states of the even-A Sn isotopes as a function of the neutron number are shown in Fig. 10 to facilitate the discussion. They were obtained from spherical self-consistent Hartree-Fock-Bogoliubov (HFB) calculations employing the finite-range density-dependent Gogny force and were presented in Ref. [20]. The empirical single-particle g factors for all relevant neutron orbitals, deduced from measured g factors of one-quasiparticle states in odd-A Sn isotopes [21], are summarized in Table VII. Included in Table VII are also the empirical g factors of the different two-neutron configurations that can contribute to the wave function of the 2_1^+ state.

For the lightest Sn isotope under study, ^{112}Sn, the $g_{7/2}$ orbital is closest to the Fermi level (see also Fig. 4 in Ref. [15]), and therefore the $g_{7/2}^2$ and the $d_{5/2}g_{7/2}$ two-neutron configurations are expected to contribute significantly to the formation of the first excited 2^+ state. Both configurations have positive g factors around $+$ 0.2, consistent with the experimental finding of a positive $g(2_1^+)$ in this isotope. In light of Fig. 10 no dramatic changes are expected for ^{114}Sn as compared to ^{112}Sn, and indeed, no significant change in $g(2_1^+)$ is observed. It is interesting to note that in a more schematic picture with a pronounced subshell closure at $N = 64$, as discussed, for example, in Ref. [11], the 2_1^+ state in ^{114}Sn would have to be based on excitations across $N = 64$, namely, $g_{7/2}^{-1}d_{3/2}$ and $d_{5/2}^{-1}s_{1/2}$ with empirical g factors of $+$ 0.04 and -0.20, respectively. The experimental results seem to favor the more realistic picture of slowly changing occupancies rather than pronounced subshell closures. Moving to ^{116}Sn, both the $d_{3/2}$ and $s_{1/2}$ orbitals are already nearly half filled, so that the $d_{3/2}s_{1/2}$ configuration ($g = -0.11$) becomes an additional

TABLE VII. Empirical single-particle g factors for the neutron orbitals in the $N = 50$–82 major shell and selected proton orbitals relevant for proton core excitations across $Z = 50$ and resulting empirical g factors of two-quasiparticle configurations with $J^\pi = 2^+$.

Single-particle g factors		2_1^+ state configurations	
Orbit	$g_{\rm emp}$	Configuration	$g_{\rm emp}$
$\nu d_{5/2}$	-0.43	$\nu d_{5/2}g_{7/2}$	$+0.23$
$\nu g_{7/2}$	$+0.18$	$\nu d_{5/2}^{-1}s_{1/2}$	-0.20
$\nu s_{1/2}$	-1.8	$\nu d_{3/2}s_{1/2}$	-0.11
$\nu d_{3/2}$	$+0.46$	$\nu g_{7/2}^{-1}d_{3/2}$	$+0.04$
$\nu h_{11/2}$	-0.25		
$\pi g_{9/2}$	$+1.22$	$\pi g_{9/2}d_{5/2}$	1.09
$\pi d_{5/2}$	$+1.38$	$\pi g_{9/2}g_{7/2}$	1.34
$\pi g_{7/2}$	$+0.73$		

option to form the 2_1^+ state, while the $g_{7/2}^2$ and $g_{7/2}d_{5/2}$ configurations lose importance due to the large degree of filling of the $g_{7/2}$ and $d_{5/2}$ orbitals. This may be the reason behind the observed decrease of $g(2_1^+)$ between ^{114}Sn and ^{116}Sn. The positive experimental g factor for the 2_1^+ state in ^{118}Sn has been attributed in Ref. [11] to the influence of the $d_{3/2}^2$ configuration ($g = +0.46$), which, following the occupancies shown in Fig. 10, is certainly expected to compete with the $d_{3/2}s_{1/2}$ configuration ($g = -0.11$) in forming the 2_1^+ state. The $g_{7/2}$ and $d_{5/2}$ orbitals are, instead, already nearly blocked in ^{118}Sn. Unfortunately, in the present work, ^{118}Sn has not been studied, and therefore the experimental value is still tainted with a relatively large uncertainty. Finally, for the isotopes above $A = 120$, the $h_{11/2}$ orbital ($g = -0.25$) is being filled and therefore is expected to play a dominant role in addition to the configurations $d_{3/2}^2$ and $d_{3/2}s_{1/2}$ ($g = +0.46$ and $g = -0.11$). Again, this expectation based on simple arguments is found to be in qualitative agreement with the experimental results, namely, the negative $g(2_1^+)$ values obtained for ^{120,122,124}Sn. However, in particular for the heaviest isotopes under study, the large deviation of the experimental values ($g = -0.044(19)$ in ^{122}Sn and $g = -0.067(14)$ in ^{124}Sn) from the empirical g factor of the $h_{11/2}$ orbital ($g = -0.25$) is surprising considering that for these isotopes there are virtually no alternatives to the $h_{11/2}^2$ configuration in the formation of the 2_1^+ state. There is one ingredient we so far ignored in our discussion but which becomes important once the $h_{11/2}$ orbital gets involved, nuclear pairing. It is known that the pairing energy is largest for high-j shells such as $h_{11/2}$, and the pairing energy of a pair of nucleons in a nearly empty shell is particularly large. In ^{122,124}Sn, the $h_{11/2}$ orbital only slowly starts to get filled. To break one of the few pairs in this orbital to form the 2_1^+ state requires a considerable amount of energy. An alternative mechanism that may well compete is the excitation of a neutron pair from the $d_{3/2}$ to the $h_{11/2}$ orbital with the coupling of the remaining two $d_{3/2}$ neutrons to $J = 2$. In both scenarios the $d_{3/2}$ orbital does not contribute to the total pairing energy because it is either completely filled or contains one pair aligned to $J = 2$. With respect to the $h_{11/2}$ orbital, however, the situation is very different. In the case of the neutron pair excitation the pairing energy of two neutron pairs in the $h_{11/2}$ shell, namely, the one excited from the $d_{3/2}$ orbital and the one that in this case does not have to be broken to form the 2_1^+ state, is gained. A detailed calculation of the relative contributions of these two alternatives in the formation of the 2_1^+ state in the heavy Sn isotopes, which depend on both the single-particle and the pairing energies, is beyond the scope of this qualitative discussion. However, given the positive g factor of the $d_{3/2}^2$ configuration ($g = +0.46$), we can estimate that a 25%–30% contribution of this configuration would account for the experimentally observed $g(2_1^+)$ values in ^{122,124}Sn.

So far, only neutron contributions to the 2_1^+ state have been discussed. Now we will examine the possible contribution of core-excited proton configurations, such as $g_{9/2}^{-1}d_{5/2}$, proposed as an explanation of the observed excess in $B(E2)$ strength in the lighter Sn isotopes, as discussed in the Introduction. First of all, it should be mentioned that the reported increase in the $B(E2)$ values between midshell ^{116}Sn and its lighter neighbors ^{112,114}Sn [7,9], which motivated the experiments presented here, was not confirmed by the measured lifetimes as discussed in detail in [15]. With respect to the $g(2_1^+)$ values in ^{112,114}Sn, the experimental results are in agreement with or even smaller than expectations based exclusively on different contributing neutron configurations, thus leaving little room for proton configurations, all characterized by large positive empirical g factors (compare Table VII).

Concerning the 4_1^+ and 3_1^- states studied in this work, the relatively large experimental uncertainties do not motivate a very detailed discussion. However, it is interesting to note that the $g(4_1^+)$ values seem to follow a trend similar to the g factors of the 2_1^+ states. In general, the experimental values for both states are all within the range of the empirical g factors of the configurations expected to contribute to the wave functions of these states. For the 4_1^+ state these are mainly the $g_{7/2}^2$ ($g = +0.18$), $d_{5/2}g_{7/2}$ ($g = -0.02$), $g_{7/2}d_{3/2}$ ($g = +0.24$), and $g_{7/2}s_{1/2}$ ($g = -0.07$) configurations, while for the 3_1^- state the $h_{11/2}g_{7/2}$ ($g = -0.39$) and $h_{11/2}d_{5/2}$ ($g = -0.14$) configurations are expected to dominate.

B. Shell-model calculations

Two different shell-model (SM) calculations have been performed in the present work. In the first the $1d_{5/2}$, $0g_{7/2}$, $2s_{1/2}$, $1d_{3/2}$, and $0h_{11/2}$ neutron orbitals have been considered as particle valence space outside a closed ^{100}Sn core, while in the second the same orbitals served as space for neutron holes with respect to a ^{132}Sn core. The first calculation is based on the N3LO nucleon-nucleon interaction tailored to a ^{100}Sn core. For details of this approach we refer the reader to Ref. [8], in which the resulting $B(E2)$ transition strengths to the first excited 2^+ states in the even-A Sn isotopes have been discussed. The second SM calculation performed in the present work employs the CD-Bonn interaction tailored to a ^{132}Sn core and experimental single-hole energies, which are taken from ^{131}Sn for all considered orbitals [22]. This second calculation is in line with the ones presented in Refs. [23,24] to describe low-lying levels in ^{127,129}Sn as well as g factors of excited states in $^{124-130}$Sn. Both calculations have been performed with the CENS software [25] and the g factors for free nucleons have been employed in the calculation of magnetic moments.

The results of the two calculations are compared to the experimental values in Fig. 9. The calculation with a ^{100}Sn core very nicely reproduces the general trend of the measured g factors from positive values in ^{112,114}Sn to negative values in the heavier isotopes. The most significant deviation is observed for ^{122,124}Sn, where values closer to the $h_{11/2}$ single-particle g factor ($g = -0.25$) are obtained in the SM calculation as compared to experiment. The origin of this discrepancy may be the underestimation of neutron pair excitations from the $d_{3/2}$ to the $h_{11/2}$ orbital, as discussed above. In the case of the SM calculation with a ^{132}Sn core the description of the experimental data is worse. Negative g factors are predicted for the whole chain of isotopes between ^{112}Sn and ^{124}Sn, in contrast to the experimental findings. While this approach has been proven to nicely reproduce the properties of Sn isotopes closer to the ^{132}Sn core, it seems to fail in the description of the Sn nuclei in the lower half of the major neutron shell. One possible reason may be an incorrect

description of the evolution of the effective single-particle energies across the $N = 50$–82 shell. Interestingly, in this SM calculation the wave function of the 2_1^+ state contains already in ^{112}Sn on average 2.7 neutrons in the $h_{11/2}$ orbital, while the corresponding number in the calculation with the ^{100}Sn core is 0.7, in accordance with the HFB calculation shown in Fig. 10. It is therefore most probably the contribution of the $\nu h_{11/2}^2$ configuration to the 2_1^+ state that leads to negative g factors for the 2_1^+ states in ^{112,114}Sn in the SM calculation with a ^{132}Sn core.

For completeness we also include in Fig. 9 the g factor predictions from calculations using the relativistic and nonrelativistic quasiparticle random phase approximations (RQRPA and QRPA) as reported in the literature [26–28]. The QRPA calculation is in overall agreement with the experimental data for the heavier isotopes but does not reproduce the positive g factors obtained for ^{112,114}Sn. The RQRPA calculations, on the other hand, predict decreasing but positive g factors for all stable isotopes in contrast to the experimental results. For a discussion of the origin of the difference between these two calculations we refer the reader to Ref. [11].

VI. SUMMARY AND CONCLUSIONS

The g factors of the 2_1^+ states in the stable Sn isotopes with $A = 112, 114, 116, 122, 124$ have been measured with high accuracy using the transient-field technique in conjunction with Coulomb excitation in inverse kinematics and a highly efficient γ-ray detection setup consisting of four EUROBALL cluster detectors. The experimental results have been discussed qualitatively on the basis of empirical single-particle g factors and compared to two different large-scale SM calculations using ^{100}Sn and ^{132}Sn as inert cores and to QRPA and RQRPA calculations. The SM calculation with a ^{100}Sn core has been found to best describe the experimental g factors. The experimental $g(2_1^+)$ values in ^{122,124}Sn are considerably smaller than the empirical g factor of the $\nu h_{11/2}^2$ configuration, which is expected to dominate the wave function of the 2_1^+ state in these isotopes. This observation may point to the importance of neutron pair excitations from the $d_{3/2}$ to the $h_{11/2}$ orbital in the formation of this state. The measured $g(2_1^+)$ in ^{112,114}Sn are reasonably well reproduced within a pure neutron valence space and do not point to a significant contribution of proton-core-excited configurations to the wave function of the 2_1^+ state in these isotopes. Finally, in view of the established excess of $E2$ strength in the lighter Sn isotopes with $A = 106, 108, 110$ it certainly would be very interesting to measure the 2_1^+ g factor in one of these isotopes using radioactive ion beams. We believe that such experiments will come into reach in the near future at facilities such as REX-ISOLDE and TRIUMF.

ACKNOWLEDGMENTS

This work has been supported by the Spanish Ministerio de Ciencia e Innovación under Contracts No. FPA2007-66069 and No. FPA2009-13377-C02-02, the Spanish Consolider-Ingenio 2010 Programme CPAN (Contract No. CSD2007-00042), and the German BMBF under Grant No. 06DA214I. J. Walker acknowledges financial support from the Universidad Autónoma de Madrid. Finally, we would like to thank the GSI accelerator team for their effort to provide high-quality beams.

[1] I. Talmi, Nucl. Phys. A **172**, 1 (1971).
[2] I. Talmi, *Simple Models of Complex Nuclei*, (Harwood Academic Publishers, Chur, Switzerland, 1993).
[3] A. Banu *et al.*, Phys. Rev. C **72**, 061305(R) (2005).
[4] J. Cederkäll *et al.*, Phys. Rev. Lett. **98**, 172501 (2007).
[5] J. N. Orce *et al.*, Phys. Rev. C **76**, 021302(R) (2007); **77**, 029902(E) (2008).
[6] C. Vaman *et al.*, Phys. Rev. Lett. **99**, 162501 (2007).
[7] P. Doornenbal *et al.*, Phys. Rev. C **78**, 031303(R) (2008).
[8] A. Ekström *et al.*, Phys. Rev. Lett. **101**, 012502 (2008).
[9] R. Kumar *et al.*, Phys. Rev. C **81**, 024306 (2010).
[10] M. Hass, C. Broude, Y. Niv, and A. Zemel, Phys. Rev. C **22**, 97 (1980).
[11] M. C. East *et al.*, Phys. Lett. B **665**, 147 (2008).
[12] C. Teich *et al.*, Phys. Rev. C **59**, 1943 (1999).
[13] A. Jungclaus *et al.*, Phys. Rev. Lett. **80**, 2793 (1998).
[14] J. Leske *et al.*, Phys. Rev. C **74**, 024315 (2006).
[15] A. Jungclaus *et al.*, Phys. Lett. B **695**, 110 (2011).
[16] K.-H. Speidel, O. Kenn, and F. Nowacki, Prog. Part. Nucl. Phys. **49**, 91 (2002).
[17] Brookhaven National Nuclear Data Center (NNDC), [http://www.nndc.bnl.gov/ensdf/].
[18] A. E. Stuchbery *et al.*, Nucl. Phys. A **435**, 635 (1985).
[19] M. P. Robinson *et al.*, Nucl. Phys. A **647**, 175 (1999).
[20] M. Anguiano *et al.*, Phys. Lett. B **545**, 62 (2002); J. L. Egido (private communication).
[21] N. J. Stone, At. Data Nucl. Data Tables **90**, 75 (2005).
[22] B. Fogelberg *et al.*, Phys. Rev. C **70**, 034312 (2004).
[23] H. Gausemel *et al.*, Phys. Rev. C **69**, 054307 (2004).
[24] L. Atanasova *et al.*, Eur. Phys. Lett. **91**, 42001 (2010).
[25] T. Engeland, M. Hjorth-Lensen, and G. R. Jansen, The CENS software, a Computational Environment for Nuclear Structure, [http://www.fys.uio.no/compphys/cp/software.html].
[26] A. Ansari, Phys. Lett. B **623**, 37 (2005).
[27] A. Ansari and P. Ring, Phys. Rev. C **74**, 054313 (2006).
[28] J. Terasaki, Nucl. Phys. A **746**, 583c (2004).